ROYAL SOCIETY OF CHEMISTRY

PAPER

Check for updates

Highly efficient (EQE > 27%) Yellow OLEDs using spiro[fluorene-9,9′-phenanthren-10′-one]-carbazole-based donor–acceptor–donor host materials†

Yu Hsuan Lin,[a] Wei-Han Lin,‡[b] Yi-Sheng Huang,‡[c] Chen-Hsun Wu,[b] Premkumar Gnanasekaran,[a] Yi-Min Chang,[a] Sheng-Wei Teng,[c] Chin-Wei Lu, [ID] *[c] Chih-Hao Chang [ID] *[b] and Yuan Jay Chang [ID] *[a]

Four bipolar host materials, with spiro[fluorene-9,9′-phenanthrene-10′-one] acceptors with nitrile fragments and *ortho*, *para*-phenyl carbazole, and triphenylamine as donor fragments, namely **MS-CN**, **MS-OC**, **MS-PC**, and **MS-TPA**, respectively, were designed, synthesized, and their photophysical and electrochemical studies were investigated. All **MS**-host materials exhibited adequate energy gaps, making them suitable candidates for use as host materials for green, yellow, and red phosphorescent organic light-emitting diodes (OLEDs). We have also designed a series of OLED devices with three different emitting layered architectures to explore their potential in electroluminescence applications. Among the devices using **MS-OC**, the CN-T2T-blended cohost achieved the highest efficiency among the tested yellow-emitting OLEDs, having a luminance efficiency of 80.0 cd A^{-1}, power efficiency of 113.0 lm W^{-1}, low turn-on voltage of 2.1 V, high maximum luminance of 142464 cd m^{-2}, and peak EQE of 27.1%. The maximum efficiency of the device is one of the highest values reported in the literature for PO-01-based devices, demonstrating the high potential of our molecular design for host materials.

1. Introduction

Organic light-emitting diodes (OLEDs) from transition-metal-based phosphors with efficient triplet exciton harvesting can achieve 100% internal quantum efficiency (IQE) through heavy-atom-enhanced strong spin–orbit coupling, thus facilitating extensive development in the fields of displays and solid-state lighting devices.[1–3] Regardless of the ongoing research and achievements in high-performance phosphorescent OLEDs (PhOLEDs), much room remains for the improvement of their efficiency and brightness.[4–13] Typically, the emitting layer (EML) of PhOLEDs is configured with an emitter as a guest

homogeneously dispersed in a suitable organic host material to reduce the chances of triplet–triplet annihilation to enhance the efficiency of the device.[14–16] For maximum exciton harvesting as phosphorescence emission, the host materials should possess (i) large ΔE_{ST}, (ii) higher lying singlet (S1) and triplet levels (T1) than guest materials to have better Förster resonance energy transfer (FRET) and Dexter energy transfer (DET),[8] (iii) better energy level matching for efficient charge injection into the guest molecules,[17] and (iv) a high glass transition temperature (T_g) and thermal decomposition temperature (T_d) to ensure thermal stability.[18,19] There is a high demand for excellent host materials for efficient PHOLEDs with the above-mentioned thermal stability and photophysical and electrochemical properties, which continues to be a challenging task.[20,21]

In 2021, we reported **MS**-host materials (**MSs**) with a spiro-[fluorene-9,9′-phenanthren-10′-one] moiety for high-efficiency perovskite solar cells (PSCs) with a device architecture, ITO/NiO$_x$/**MSs**/perovskite/PC$_{61}$BM/BCP/Ag. **MSs** were utilized as the interfacial layer, and the surface appearance of NiO$_x$ was improved. The characteristics of NiO$_x$/**MSs** on the perovskite layer, quantified in terms of the photoluminescence (PL), were better than those of bare-NiO$_x$ in terms of the hole-transport ability and power conversion efficiency. The power efficiency reached 20.34%, comparable to polycrystalline silicon solar

[a] *Department of Chemistry, Tunghai University, No. 1727, Sec. 4, Taiwan Boulevard, Xitun District, Taichung 40704, Taiwan. E-mail: jaychang@thu.edu.tw; Tel: +886-4-23590121-32224*

[b] *Department of Electrical Engineering, Yuan Ze University, Chungli 32003, Taiwan. E-mail: chc@saturn.yzu.edu.tw; Tel: +886-3-4638800-7517*

[c] *Department of Applied Chemistry, Providence University, Taichung 43301, Taiwan. E-mail: cwlu@pu.edu.tw; Tel: +886-4-26328001-15213*

† Electronic supplementary information (ESI) available: The ^{1}H and ^{13}C NMR spectra of all compounds, mass spectra, TDDFT calculated orbitals, thermogravimetric analysis (TGA) of HTMs, differential scanning calorimetry (DSC), OLED device **A** and device **C** performances. See DOI: https://doi.org/10.1039/d2tc05296b
‡ Equal contribution first author.

This journal is © The Royal Society of Chemistry 2023

J. Mater. Chem. C, 2023, **11**, 3101–3111 | **3101**

cells (16%). The NiO$_x$/**MS-OC** PSCs had good thermal stability and retained the original power conversion efficiency of 93.16% even after 370 days under argon (25 °C). Furthermore, **MS** host exhibited suitable highest occupied molecular orbital (HOMO) (ranging from −5.18 to −5.27 eV) and lowest unoccupied molecular orbital (LUMO) (ranging from −1.94 to −2.98 eV) energy levels, as well as high triplet energy levels with large ΔE_{ST}, indicating their potential as host materials.

In this study, we report four host materials, namely **MSs**, based on spiro-[fluorene-9,9′-phenanthren-10′-one] moiety with *ortho*-, *para*-phenyl carbazole, and triphenylamine as a donor fragment (control nitrile fragment) satisfying the following requirements: (i) suitable HOMO and LUMO energy levels as well as triplet energies; (ii) adequate charge mobilities; (iii) low cost (18–22 USD g^{-1}) and simple synthesis (three to five steps for acquiring **MS**-host materials). The last point was the most critical point we focused on for developing this series because the cost determines the market acceptance of materials. **MS**-host materials were constructed using spiro[fluorene-9,9′-phenanthrene-10′-one] core configurations decorated with different donor moieties as follows: *para*-connected cyano groups for **MS-CN**, *para*-connected triarylamine moieties for **MS-TPA**, *para*-connected phenyl-carbazole moieties for **MS-PC**, and *ortho*-connected phenyl-carbazole moieties for **MS-OC**. The HOMO and LUMO energy levels of this series of target molecules are in the ranges of −5.1 to −5.3 eV and −1.8 to −2.4 eV, respectively. The adequate triplet energies (2.47–2.66 eV) of these **MSs** allowed them to serve as ideal host materials for phosphorescent emitters of green Ir(ppy)$_3$, yellow PO-01, and red Ir(piq)$_2$(acac). Furthermore, we fabricated three different device architectures using different EML structures with **MSs** materials designed to seek balanced electron–hole recombination. We used **MS**-host materials in three combinations with phosphorescent dopants as EML layers in the OLED devices as follows: a single EML based on a single host material (*i.e.*, **MSs** only) for the **A** series devices, a single EML with a blended host (*i.e.*, **MSs** mixed with 3′,3‴,3‴′′-(1,3,5-triazine-2,4,6-triyl)tris(([1,10-biphenyl]-3-carbonitrile)) (CN-T2T) (1:1)) for the **B** series devices, and double EMLs with a single host (*i.e.*, TCTA) and a blended host (*i.e.*, **MSs** mixed with CN-T2T (1:1)) for the **C** series devices. Overall, the external quantum efficiency (EQE) of the **B** and **C** series devices using cohost EML structures exceeded the **A** series device with the EML using a single host material, which was attributed to the excellent carrier balance in the **B** and **C** series devices. Significantly, the spiro[fluorene-9,9-phenanthren-10-one] core was decorated with phenyl-carbazole donor moieties in the *ortho*-orientation (*i.e.*, **MS-OC**), resulting in a densely packed structure according to the single-crystal experiments. As indicated, organic light-emitting diodes (OLEDs) adopting **MS-OC** as the host material exhibited the best efficiency among the three device types, regardless of the emitter employed. In the **A** series device with a single host material structure, the maximum efficiency of the **MS-OC**-based device with the yellow-emitting PO-01 achieved 22.5% (67.1 cd A^{-1} and 81.1 lm W^{-1}). Moreover, the respective peak efficiencies of 27.1% (80.0 cd A^{-1} and 113.0 lm W^{-1}) and

22.3% (78.2 cd A^{-1} and 111.1 lm W^{-1}) were obtained for the yellow- and green-emitting **MS-OC** devices in the **B** series. It is worth mentioning that the yellow-emitting device's performance in the **B** series made an excellent breakthrough as compared with the peak efficiencies of 25.3% (77.2 cd A^{-1} and 59.8 lm W^{-1}) for a typical PO-01-based device.[22] These outcomes show that **MSs** could effectively regulate the carrier balance *via* mixing with appropriate electron-transport materials to realize highly efficient PhOLEDs, further underscoring the great potential of this molecular design.

2. Results and discussion

2.1 Synthesis of MSs

The structures of **MS**-host materials are shown schematically in Fig. 1 and their synthesis procedures are presented in Scheme S1 (ESI†). The **MSs** contain two side substituents (cyano, arylamine, and carbazole) at the core moiety of spiro[fluorene-9,9′-phenanthren-10′-one]. For each of the **MSs**, the synthesis was initiated using 2,7-dibromo-10′H-spiro[fluorene-9,9′-phenanthren]-10′-one (**1**), yielding **MS-CN** through the cyanation reduction with CuCN.[23] The final products of **MS-TPA**, **MS-OC**, and **MS-PC** were obtained *via* the Suzuki–Miyaura coupling reactions with high yields (total yield 63–90%), and were easily purifiable.[24] Detailed descriptions of the synthesis procedures and nuclear magnetic resonance (NMR) data (Fig. S1–S3) are presented in the ESI.†

2.2 Photophysical properties

The ultraviolet-visible absorption, fluorescence, and phosphorescence emission spectra of all **MSs** were obtained in a toluene solution, and the corresponding spectral profiles and numerical data are shown in Fig. 2(a) and Table 1. **MS-CN** and **MS-OC** exhibited higher energy absorption bands in the 280–340 nm range, which were attributed to the high π–π* transitions of the core moiety of spiro[fluorene-9,9′-phenanthren-10′-one] and the weak red-shift absorption for **MS-OC** at 340 nm, owing to the addition of *ortho*-phenyl-carbazole at the core moiety of
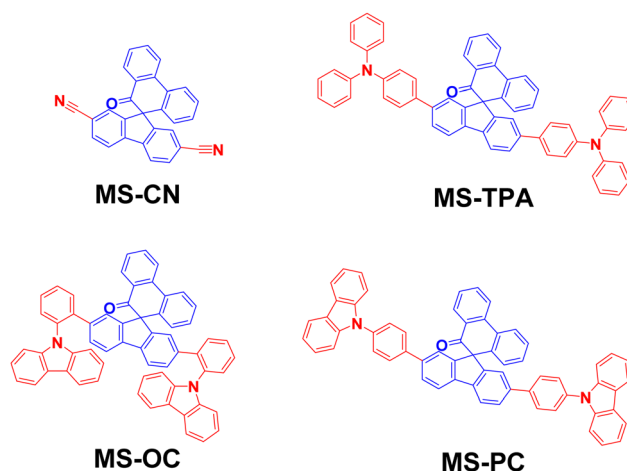

Fig. 1 Chemical structures of the studied **MS**-host materials.

3102 | *J. Mater. Chem. C*, 2023, **11**, 3101–3111

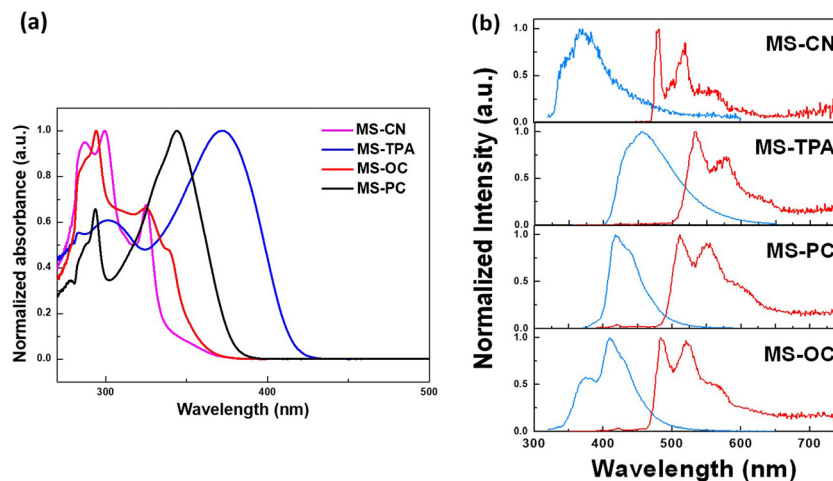This journal is © The Royal Society of Chemistry 2023

Fig. 2 (a) Absorption spectra. (b) Fluorescence and phosphorescence spectra of **MS-CN**, **MS-TPA**, **MS-PC**, and **MS-OC** obtained in a toluene solution.

Table 1 Photophysical characteristics of the tested MSs compounds

Material	λ_{abs} (nm)	HOMO[a] (eV)	LUMO[b] (eV)	Fl_{em}^{c} (nm)	$S_1{}^{b}$ (eV)	Ph[c] (nm)	$T_1{}^{c}$ (eV)	QY[d] (%)
MS-CN	286, 298, 324	−5.12	−1.81	345, 370, 383 (sh)	3.55	481, 520, 553 (sh)	2.63	43
MS-TPA	282, 300, 372	−5.30	−2.40	432 (sh), 455	3.07	533, 578	2.47	83
MS-OC	294, 324, 338 (sh)	−5.20	−1.81	376, 410, 430 (sh)	3.31	484, 520, 562 (sh)	2.66	94
MS-PC	293, 334 (sh), 343	−5.19	−2.08	418, 436 (sh)	3.14	511, 550, 595 (sh)	2.55	90

[a] Estimated from the CV curve. [b] Estimated from LUMO calculated by HOMO + E_{0-0} (E_{0-0} was determined from the onset of the UV-Visible spectra in toluene). [c] Estimated from the onset of the fluorescence and phosphorescence measured in toluene. [d] Photoluminescence quantum yield of 5 weight percent PO-01 doped in **MS-CN**, **MS-TPA**, **MS-PC**, and **MS-OC** films.

spiro[fluorene-9,9′-phenanthren-10′-one]. In contrast, **MS-TPA** and **MS-PC** showed major red-shifted broad absorption peaks at 372 and 343 nm, respectively, owing to the addition of the electron-donating triphenylamine and phenyl carbazole at the *para*-position of the core moiety, which increased the coplanarity and conjugation of the molecular backbone. **MS-TPA** exhibited a more red-shifted absorption peak, which was mainly attributed to the strong electron-donating nature of triphenylamine, which destabilized the HOMO energy level as compared with phenyl carbazole.

We also studied the PL properties of the prepared **MSs** in a toluene solution, and the corresponding emission profiles and spectral data are shown in Fig. 2(b) and Table 1. All of the studied **MSs** showed broad and structured violet to deep-blue fluorescence (S₁) emission at ambient temperature. Among all the studied host materials, **MS-CN** exhibited violet emission at 370 nm because of the strong electron-withdrawing dicyano group substituted at the core moiety of spiro[fluorene-9,9′-phenanthren-10′-one], while **MS-OC** exhibited a structured emission maximum at 410 nm with a shoulder peak at 376 nm. On the other hand, **MS-PC** and **MS-TPA** showed broad and red-shifted emission maxima at 455 and 418 nm, respectively, owing to their strong electron-donating characteristics, and the free rotation through the molecular backbone of triphenylamine showed broad and red-shifted emission as compared with phenyl carbazole. Moreover, all of the studied

host materials showed highly structured phosphorescence (T₁) emission profiles in toluene solution at −77 K. The energy levels were calculated based on the fluorescence (S₁) and phosphorescence (T₁) emission onset data, and the resulting values for the corresponding energy gaps are listed in Table 1. The triplet energy gaps of these compounds imply that the synthesized **MSs** are promising as host materials for phosphorescent OLEDs. On the other hand, thin-film samples of 5-weight percent PO-01 doped in **MSs** materials were prepared to determine the PL quantum yields (PLQYs). The PLQY values of the doped film samples were evaluated as 0.43 (**MS-CN**), 0.83 (**MS-TPA**), 0.94 (**MS-PC**), and 0.90 (**MS-OC**). The high PLQY values obtained in the last two samples revealed their potential for electroluminescence (EL) applications.

2.3 Thermal stability and electrochemical properties

The thermal properties of the host materials were determined using thermogravimetric analysis (TGA) and differential scanning calorimetry (DSC) at a heating rate of 10 °C min⁻¹; the spectra are shown in Fig. S4 and S5 (ESI†). **MS-CN**, **MS-TPA**, and **MS-PC** all exhibited a flat line in their DSC spectra for the glass transition temperature (T_g), which was attributed to the poor crystallinity and poor stacking interactions; this is supported by the conclusions of our previously reported X-ray studies, except for **MS-OC** (T_g = 179 °C).[24] The thermal decomposition temperatures (T_d) of **MS-CN**, **MS-PC**, **MS-OC**, and **MS-TPA** were 352,

This journal is © The Royal Society of Chemistry 2023

J. Mater. Chem. C, 2023, 11, 3101–3111 | 3103

396, 426, and 475 °C, respectively, as shown in Fig. S4 (ESI†). This suggests that the studied host materials exhibit excellent thermal stability, which is advantageous for OLED fabrication by thermal vacuum deposition.

Cyclic voltammetry studies of all **MS**-host materials revealed reversible oxidation curves, as shown in Fig. S6 (ESI†) and the data summarized in Table 1. The onset of ICT transition bands determined the zero–zero energy, and was used to further calculate the LUMO energy level in Fig. 2(a). **MS-TPA** has the smallest energy gap (2.9 eV), which is attributed to the strong electron-donating moiety; this result is also consistent with the UV-vis and PL data. **MSs** have low HOMO and high LUMO levels, and the energy gap is between 2.9 and 3.39 eV in Fig. 3. This indicated that all **MSs** are suitable as host materials for the yellow emitter PO-01 and the red emitter Ir(piq)$_2$acac.

2.4 Computational analysis

To gain further insight into the properties of the optimized structures, the electrostatic potential (ESP) map and the frontier energy level information of **MSs** were obtained using time-dependent density functional theory (TD-DFT) calculations, using the B3LYP/6-31G(d) basis set in Gaussian 16 W; the results are shown in Fig. S7, S8 (ESI†) and the numerical values are listed in Table S1 (ESI†). As shown in Fig. S8 (ESI†), the optimized structure of **MSs** exhibited structural conformations, with a dihedral angle between the acceptor core and phenyl spacer and donor fragment. **MS-CN** is a simple spiro-core moiety with an electron-withdrawing nitrile group substituted on a fluorene fragment and without a donor. The electrostatic potential map shows that the positive ESP was localized on the phenyl rings while negative ESP was localized on the electron-withdrawing carbonyl and nitrile fragments. The calculated frontier molecular orbitals suggested the inadequate separation of **MS-CN** with the HOMO (−6.83 eV) and LUMO (−2.70 eV) energy levels. For **MS-TPA**, the predicted dihedral angle between the central core of spiro[fluorene-9,9′-phenanthren-10′-one] and donor triphenylamine was 38.0°, and the electrostatic potential (ESP) map revealed that the highly negative ESP was concentrated on the carbonyl group, while positive ESP values were confined to the fluorene-triphenyl amine donor backbone. The HOMO (−5.07 eV) energy level was localized over the fluorene-triphenyl amine donor backbone while the LUMO (−2.08 eV) energy level was localized on the phenanthrene-10′-one fragment. Similarly, for **MS-PC**, the

predicted dihedral angle between the central core of spiro[fluorine-9,9′-phenanthren-10′-one] and the phenyl-carbazolyl fragment was 39.5°. The HOMO (−5.34 eV) energy level was localized on the fluorene-phenyl-carbazolyl fragment while the LUMO (−2.06 eV) energy level was localized on the phenanthrene-10′-one fragment. The ESP map showed that the positive ESP on the carbonyl group and positive ESP values were localized on the fluorene-phenyl-carbazolyl donor backbone. In contrast, **MS-OC** exhibited a highly twisted molecular structure with large dihedral angles for the central core of spiro[fluorene-9,9′-phenanthren-10′-one] and a phenyl-carbazolyl fragment, at 51.3°. The ESP map and frontier molecular orbitals (HOMO = −5.14 eV and LUMO = −2.11 eV) exhibited similar trends to **MS-TPA** and **MS-PC**.

2.5 Exciplex experiments

The four synthesized host materials were then used to fabricate OLEDs to examine their EL applications. Because all the studied compounds consisted of a single electron-deficient core decorated with two electron-donating moieties, it was expected that these compounds would possess a relatively weak electron-transporting ability. Therefore, subsequent device tests investigated the EML structures that were constructed using pure synthesized compounds or a blended host consisting of the synthesized compounds with an electron transport material. Before the EL tests, we obtained the PL spectra of the blended hosts to determine whether the mixtures exhibited exciplex formation. Herein, we chose CN-T2T as the electron transport part for the mixtures, owing to its adequate LUMO level, wide triplet energy bandgap, and good electron transport mobility.[25] Since CN-T2T with a Y-shaped molecular structure would increase the probability of producing physical intermolecular interactions for the successful formation of an exciplex, the fast-screening method was introduced to investigate the exciplex formation by obtaining the PL spectra of the donor:acceptor (D : A) blends in a relatively high-polarity solvent.[26] Four D : A (1 : 1) mixed samples, **MS-CN** : CN-T2T, **MS-TPA** : CN-T2T, **MS-PC** : CN-T2T, and **MS-OC** : CN-T2T, were prepared for the fast-screening method. The mixed samples were initially dissolved in tetrahydrofuran (THF), and then different quantities of deionized (DI) water were added to the solution to obtain the colloidal suspension.[27] Fig. 4(a) shows the PL spectra of CN-T2T, the synthesized **MSs**, and the mixtures, in pure THF and with 90% water added. Highly polar solutions can force the D/A molecules to aggregate, thereby increasing the likelihood of intermolecular interactions that stimulate exciplex formation. On comparing the PL spectra of the mixtures with those of the four synthesized molecules and CN-T2T dissolved in pure THF, the spectral profiles of the mixtures were similar to those of the synthesized molecules. When 90% DI water was added to THF, the spectra of the four corresponding blends were red-shifted as compared with those in pure THF. However, the red shift was insignificant in all cases, indicating that an exciplex could have been generated but was very weak.[26] Furthermore, the transient PL decays monitored at the emission peak were measured to study the relaxation behavior of the mixtures in
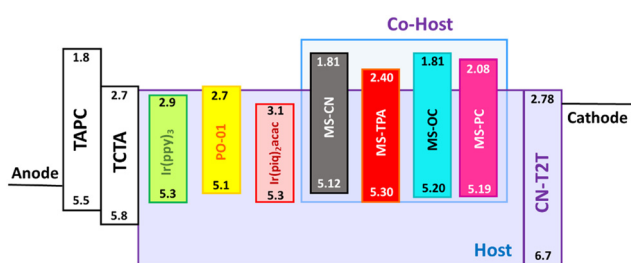

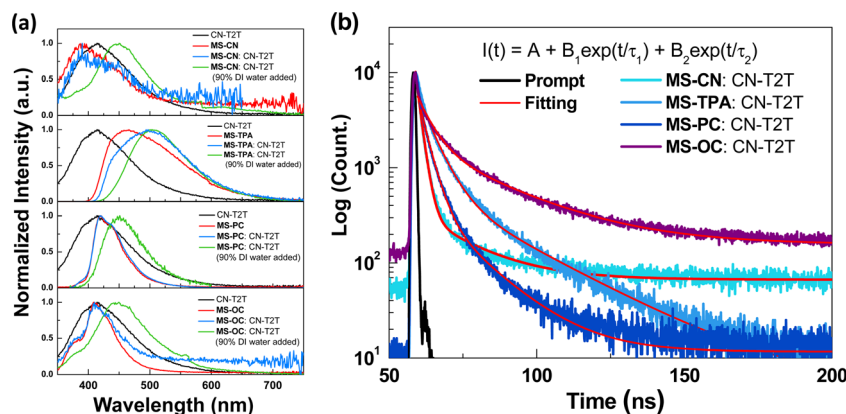Fig. 3 Energy levels for **MSs** and other materials used in OLED devices.

3104 | J. Mater. Chem. C, 2023, 11, 3101–3111

This journal is © The Royal Society of Chemistry 2023

Fig. 4 (a) Normalized PL spectra of CN-T2T, the four synthesized materials and their mixtures in pure THF and with 90% water added. (b) Transient PL profiles of the mixture samples for THF with 90% water added.

THF with 90% DI water added. Fig. 4(b) shows the excited-state decay characteristics of the four blends measured at room temperature. The formulas for the curve fitting and simulation results are presented in Table S1 (ESI†). Although these samples exhibited two-component decay profiles, both components were on the nanosecond timescale, suggesting that the excited state was dominated by fluorescence. We also made blended samples by mixing **CN-T2T** and the synthesized **MSs**. Samples A (**MS-CN**:CN-T2T, 1:1), B (**MS-TPA**:CN-T2T, 1:1), C (**MS-PC**:CN-T2T, 1:1), and D (**MS-OC**:CN-T2T, 1:1) were thin film samples composed of donor:acceptor (D:A) blends. Fig. S9 (ESI†) shows the PL spectra of the thin film samples. Again, the results indicated no exciplex emission in the four samples. The spectra of the four corresponding blends were slightly red-shifted as compared to their original PL spectra measured in toluene. In addition, the phosphorescence spectra of the samples measured at 77 K were significantly red-shifted as compared to those measured at room temperature, indicating the absence of exciplex emission. Thus, we concluded that the blended samples used as the host system in the devices should be categorized as mixed hosts rather than an exciplex hosts.

2.6 Electroluminescence properties

Because the charge mobilities of host materials adopted in OLEDs influence the performance and should be concerned before device designs, single carrier devices were fabricated to implement the space-charge-limited current (SCLC) measurements. The hole-only devices adopted the following architecture: ITO/MoO$_3$ (5 nm)/**MSs** (250 nm)/MoO$_3$ (10 nm)/Al (120 nm), for which MoO$_3$ was used as the hole injection layer and the electron blocking layer. The architecture of the electron-only devices was as follows: ITO/CN-T2T (10 nm)/**MSs** (150 nm)/CN-T2T:Li$_2$CO$_3$ 10 wt% (5 nm)/Al (120 nm), where CN-T2T and CN-T2T:Li$_2$CO$_3$ were used as the hole blocking layer and the electron injection layer, respectively.

As shown in Fig. S10 (ESI†), the J–V curves of the hole-only and electron-only devices revealed the detected current densities for **MSs**. Since the target compounds possess similar
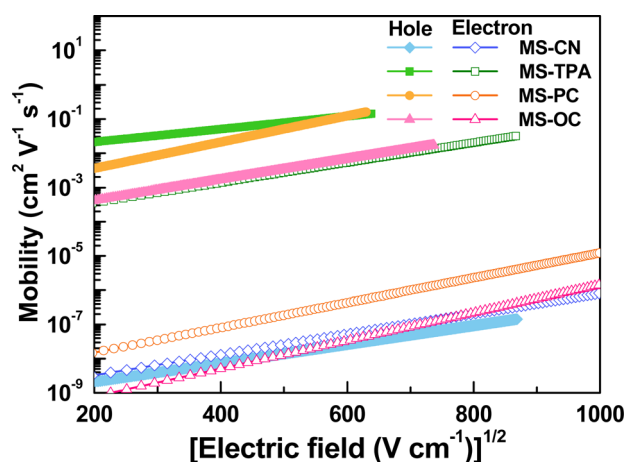

Fig. 5 Comparative field dependence mobility of **MS-CN**, **MS-TPA**, **MS-PC**, and **MS-OC**.

HOMO/LUMO levels, this result was mainly related to the charge transport conditions. The hole mobilities were estimated according to the SCLC theory ($J = 9\varepsilon\varepsilon_0\mu E^2/8L$), assuming that the evaporated organic solid films have inherently disordered morphologies. This theory states that the charge mobility dependence on the electric field is ascribed to organic semiconductors ($\mu = \mu_0 \exp(\beta E^{1/2})$), resulting in the following expression:

$$J = \left[\frac{9\varepsilon\varepsilon_0}{8L}\mu_0 \exp\left(\beta E^{1/2}\right)\right]E^2$$

where ε is the relative dielectric constant, with an approximate value of 3 for the studied materials, ε_0 is the vacuum permittivity, E is the electric field, L is the thickness of the organic film, μ_0 is the mobility at zero fields and β is the Poole–Frenkel factor. The linearization of this equation enabled the determination of μ_0 and β for the adequate high bias range. The comparative field dependence mobility of **MS-CN**, **MS-TPA**, **MS-PC**, and **MS-OC** is evidenced by the results plotted in Fig. 5. As indicated, although all **MSs** could transport both holes and electrons, these compounds presented much higher

hole mobility, exceeding the electron mobility counterpart. The hole and electron mobilities of **MS-CN** are similar and poor, which might lead to the low current density obtained in OLEDs with **MS-CN** hosts. Furthermore, comparing these curves indicates that only **MS-TPA** featured a much more balanced charge transport than the other tested compounds; that is, **MS-TPA** could be classified as a bipolar material in general. Hole mobility values were determined at a field of 0.25 MV cm^{-1} (μ(**MS-CN**) = 1.4 × 10^{-8} cm^2 V^{-1} s^{-1}, μ(**MS-TPA**) = 7.8 × 10^{-2} cm^2 V^{-1} s^{-1}, μ(**MS-PC**) = 5.0 × 10^{-2} cm^2 V^{-1} s^{-1}, and μ(**MS-OC**) = 3.3 × 10^{-3} cm^2 V^{-1} s^{-1}). On the other hand, the respective electron mobility values of **MS-CN**, **MS-TPA**, **MS-PC**, and **MS-OC** were estimated as 2.6 × 10^{-8} cm^2 V^{-1} s^{-1}, 2.7 × 10^{-3} cm^2 V^{-1} s^{-1}, 1.9 × 10^{-7} cm^2 V^{-1} s^{-1}, and 1.3 × 10^{-8} cm^2 V^{-1} s^{-1}. In addition to the host's mobility, the OLED efficiency involves multiple factors, such as charge injection, balanced charge transport, and exciton confinement. Thus, although the electron mobilities of **MS-PC** and **MS-OC** are much lower, it cannot be ruled out that devices based on these compounds may also achieve carrier balance. The results indicated that the yellow-emitting devices with **MS-PC** or **MS-OC** hosts showed satisfactory performances, which will be discussed later.

According to the mobility results of these series, most of the compounds presented higher hole transport capabilities as compared to their electron counterparts. The construction of **MSs**-based EMLs with additional electron-transporting materials was considered to boost electron transport. Therefore, to investigate this series as the hosts for constructing EMLs in OLEDs, we designed three device architectures to examine the carrier balance conditions. In addition, based on the energy bandgaps of the tested host materials, phosphorescent emitters with different energy bandgaps were chosen for fabricating red, yellow, and green OLEDs. When designing an EML, the triplet energy bandgap of the host should be higher than that of the selected emitter. Therefore, green-emitting Ir(ppy)$_3$ was used as the emitter for the host materials **MS-CN** and **MS-OC**, while yellow-emitting PO-01 and red-emitting Ir(piq)$_2$acac were doped into all synthesized host materials to construct the EML.[28–30] Two commonly used hole-transporting materials, namely, bis[(di-4-tolylamino)phenyl]cyclohexane (TAPC) and 4,4′,4″-tris(N-carbazolyl)triphenylamine (TCTA), were chosen to form step-wise hole-transport layers (HTLs), aiming to promote smooth hole injection from the HTL into the EML.[31] Moreover, as mentioned above, CN-T2T with appropriate electron transport properties was used as the electron transport layer (ETL). The three device architectures were nearly identical, except for the EML structures. The EML structures corresponding to the three devices were as follows: (1) a single EML based on a single host material for the **A** series devices, (2) a single EML with a blended host for the **B** series devices, and (3) double EMLs with a single host and a blended host for the **C** series devices. Consequently, the structures of the **A** series devices used a configuration of indium tin oxide (ITO) (90 nm)/TAPC (30 nm)/TCTA (10 nm)/**MSs** doped with an emitter (25 nm)/CN-T2T (50 nm)/LiF (1.5 nm)/Al (150 nm), where ITO and aluminum

were used as the anode and cathode, respectively. The **B** series devices with a blended host were fabricated with the following generalized architecture: ITO (90 nm)/TAPC (30 nm)/TCTA (10 nm)/**MSs**:CN-T2T (1:1) doped with an emitter (25 nm)/CN-T2T (50 nm)/LiF (1.5 nm)/Al (150 nm). In addition, the **C** series devices used a double EML configuration including a mixed EML and an auxiliary EML using a hole-transport material as the host: ITO (90 nm)/TAPC (30 nm)/TCTA (5 nm)/TCTA doped with an emitter (5 nm)/**MSs**:CN-T2T (1:1) doped with an emitter (25 nm)/CN-T2T (50 nm)/LiF (1.5 nm)/Al (150 nm). The doping concentrations for all emitters were 8 wt.% for green-emitting Ir(ppy)$_3$, 5 wt.% for yellow-emitting PO-01, and 8 wt.% for red-emitting Ir(piq)$_2$acac. To facilitate the identification of device architectures, **R**, **Y**, and **G** were added to the names of different series devices to represent different colors. In addition, the device names were also followed by adding 1, 2, 3, and 4 to represent the devices using **MS-CN**, **MS-TPA**, **MS-PC**, and **MS-OC** as hosts. For instance, the yellow-emitting device with **MS-PC** host in the **A** series devices was denoted as device **AY3**, and so on. The materials used and the schematic architecture of the fabricated OLEDs are shown in Fig. 6.

We designed three series of devices with different EML structures to investigate the carrier transport and energy transfer capabilities of the synthesized compounds from the host to the guest. Owing to the great number of devices tested, we used a histogram to present the peak EQE values of the various devices using red (**R**), yellow (**Y**), and green (**G**) emitters. Fig. 7 summarizes the peak EQE values of the **A**, **B**, and **C** series devices. The **B** and **C** series devices exhibited quite similar performances regardless of the emitter used. Still, upon closer inspection of their EL characteristics, the **B** series device with a single mixed host had the highest efficiency, while the **C** series device with an additional auxiliary EML exhibited the highest luminance. In contrast, the **A** series device with a single EML consisting of synthesized **MSs** as the host slightly underperformed as compared with the other series, indicating that these materials have slightly imbalanced carrier transport properties. Although the **A** series devices exhibited relatively low efficiency, the peak efficiencies of yellow-emitting devices **AY3** (**MS-PC**) and **AY4** (**MS-OC**) were 22.8% (66.2 cd A^{-1} and 86.0 lm W^{-1}) and 22.5% (67.1 cd A^{-1} and 81.1 lm W^{-1}), respectively, which could still be considered excellent performances for yellow emitters. Considering the host compounds with more extraordinary hole transport ability, the carrier recombination zone located at the EML/ETL interface could be expected in the device **A** series. Therefore, the carrier balance of the devices was determined by the hole transport of the host and the electron transport of the ETL in a low operation voltage range. Although **MS-TPA** possesses bipolar carrier transport ability, the lower efficiency might result from the mismatch between **MS-TPA** and CN-T2T. As for the **B** and **C** series, the hole–electron mismatch was significantly improved by blending the electron transport material CN-T2T.

Because the highest-efficiency performance was obtained for the **B** series devices, we collected the numerical data for the **B**

3106 | *J. Mater. Chem. C*, 2023, **11**, 3101–3111

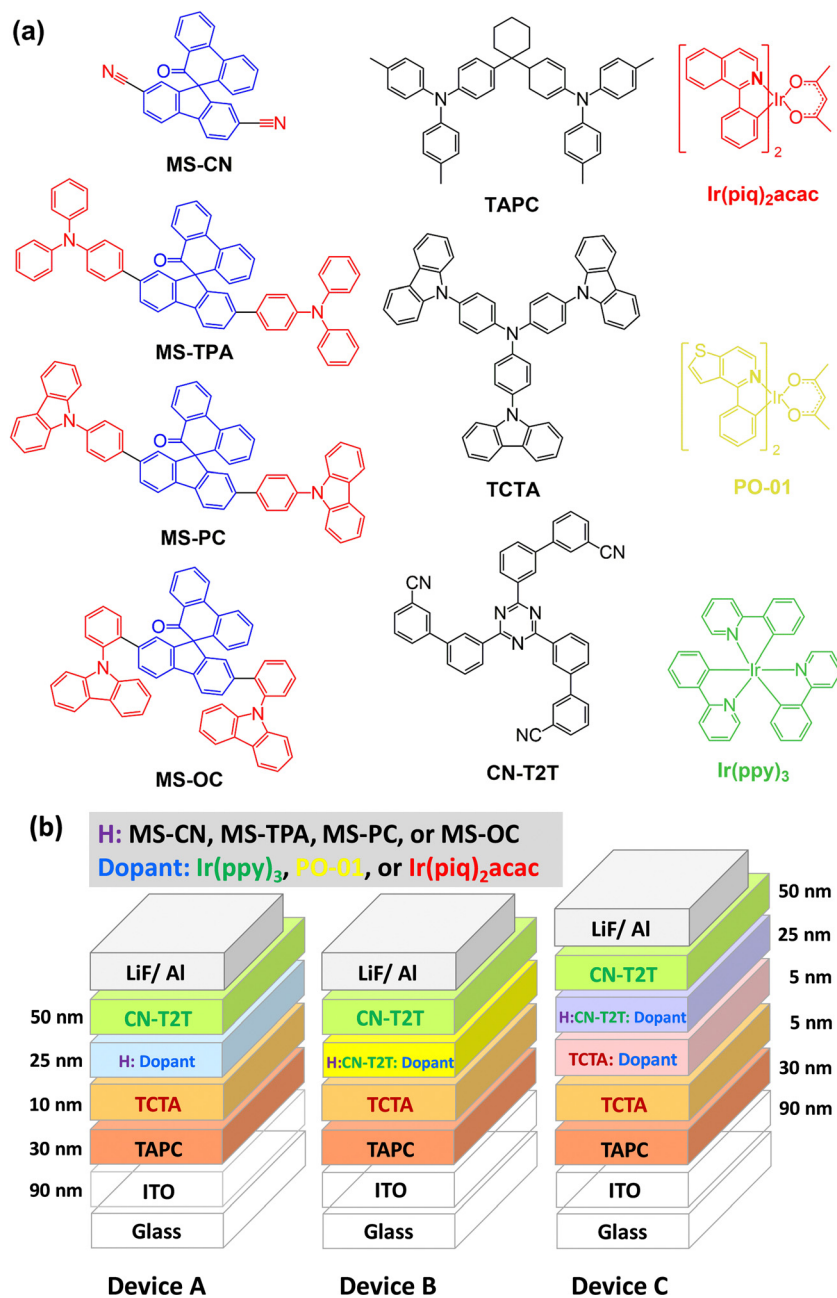This journal is © The Royal Society of Chemistry 2023

Fig. 6 (a) Schematics of the materials used in the OLEDs; (b) schematics of the fabricated OLEDs with different emitters.

Fig. 7 Peak EQEs of the tested devices for different hosts and emitters: (a) **A** series; (b) **B** series; (c) **C** series.

Table 2 EL characteristics of the **B** series devices, for different hosts and emitters

Device	BG		BY				BR			
No.	1	4	1	2	3	4	1	2	3	4
Host	MS-CN	MS-OC	MS-CN	MS-TPA	MS-PC	MS-OC	MS-CN	MS-TPA	MS-PC	MS-OC
Emitter	Ir(ppy)$_3$		PO-01				Ir(piq)$_2$acac			
External quantum efficiency^{ab} [%]	4.2 / 4.1	22.3 / 21.9	15.1 / 11.1	26.0 / 26.0	23.6 / 23.5	27.1 / 27.1	13.0 / 7.7	17.8 / 14.4	18.8 / 18.1	20.1 / 18.9
Luminance efficiency^{ab} [cd A^{-1}]	12.6 / 12.4	78.2 / 76.6	43.5 / 31.8	77.2 / 77.2	68.4 / 68.0	80.0 / 80.0	7.9 / 4.7	10.7 / 6.0	10.7 / 10.3	12.0 / 11.3
Power efficiency^{ab} [lm W^{-1}]	11.3 / 10.2	111.1 / 94.8	46.7 / 21.4	109.0 / 92.3	92.8 / 87.4	113.0 / 104.4	9.5 / 3.3	12.3 / 8.7	15.3 / 12.2	16.6 / 12.7
V_{on}^{c} [V]	2.5	2.1	2.9	2.0	2.1	2.1	2.9	2.4	2.2	2.2
$J_{1/2}$^{d} [mA cm^{-2}]	381.9	72.3	4.5	52.4	56.7	94.4	6.3	40.7	121.3	77.6
Max luminance [cd m^{-2}] [V]	36 152 [10.8]	10 6900 [9.6]	64 168 [13.0]	127 451 [11.6]	122 753 [12.0]	142 464 [10.4]	10 857 [11.4]	21 423 [12.0]	25 959 [11.2]	18 719 [10.4]
CIE1931 coordinates^b	(0.42, 0.55)	(0.34, 0.61)	(0.51, 0.48)	(0.51, 0.49)	(0.51, 0.49)	(0.51, 0.49)	(0.68, 0.31)	(0.69, 0.31)	(0.69, 0.31)	(0.69, 0.31)

^{a} Maximum efficiency. ^{b} Measured at 10^2 cd m^{-2}. ^{c} Turn-on voltage measured at 1 cd m^{-2}. ^{d} Current density at half of the peak external quantum efficiency.

series devices, including green, yellow, and red emitters from the EL characteristics, and summarized them in Table 2. For comparison, the remaining EL characteristic data for the **A** and **C** series devices are provided in the ESI† (Tables S3 and S4). Moreover, on comparing all tested emission colors for the **B** series devices, device **BY** using the yellow-emitting PO-01 showed outstanding performance; thus, it was selected as the representative case, as shown in Fig. 8. The EL characteristics of the **BR** and **BG** series devices are shown in Fig. S11 and S12 (ESI†).

Fig. 8 shows the EL characteristics of the **BY** series device with yellow-emitter PO-01, featuring a co-host-based EML consisting of **MSs** and CN-T2T. As shown in Fig. 8(a), all of the tested devices with the different host materials exhibited nearly

identical EL spectra originating from PO-01, indicating valid energy transfer from the blended host to the guest.[32] Furthermore, the emission of pure PO-01 confirmed that exciton diffusion and migration to adjacent layers were avoided.[33] This phenomenon was observed not only for the **B** series devices with different emitters but also for the **A** and **C** series devices. Accordingly, we concluded that the designed EML structures for the **A**, **B**, and **C** series devices were practical and reasonable. Fig. 8(b) shows the current density–voltage–luminance (J–V–L) curves for device BY, for different host materials. As indicated, the recorded current density curves followed the sequence **MS-CN** < **MS-TPA** < **MS-PC** < **MS-OC**, where the last two devices exhibited relatively close current densities. Similar results were obtained for the B series device with red and green
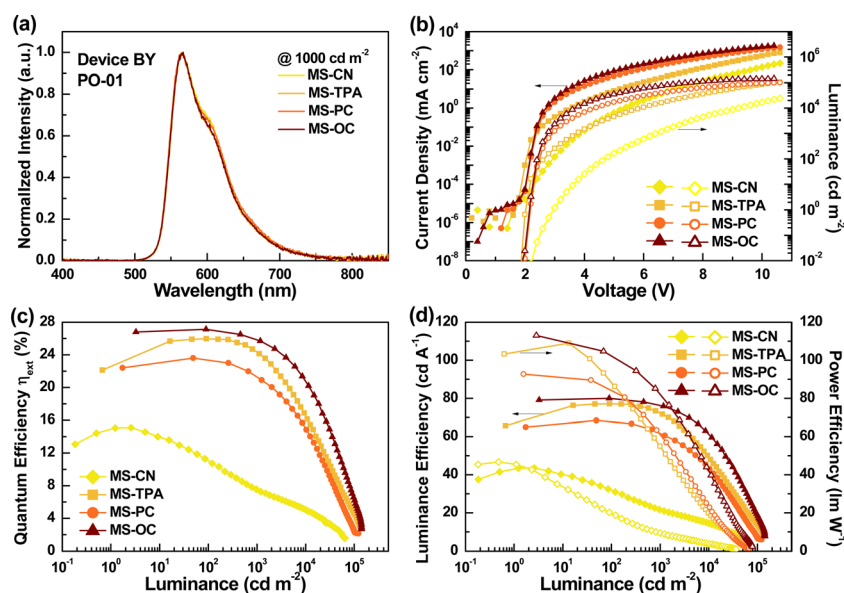

Fig. 8 (a) Normalized EL spectra at a luminance of 10^3 cd m^{-2}; (b) current density–voltage–luminance (J–V–L) characteristics; (c) EQE $vs.$ luminance; (d) luminance/power efficiency $vs.$ luminance, for devices **BY1**, **BY2**, **BY3**, and **BY4**.

3108 | J. Mater. Chem. C, 2023, **11**, 3101–3111

This journal is © The Royal Society of Chemistry 2023

emitters, or even for the A and C series devices. The low current density observed in devices with **MS-CN** hosts is reasonable, mainly due to the poor carrier transport capability of **MS-CN**. However, according to the results of SCLC experiments, **MS-TPA** has bipolar and excellent transport capability. Thus, the lower current density obtained in **MS-TPA**-based devices may be due to dopant-induced carrier imbalance or suboptimal energy transfer from host to guest. The luminance curves of the tested devices exhibited the same trends. The observed maximum luminance values for devices **BY1**, **BY2**, **BY3**, and **BY4** were 64168, 127451, 122753, and 142464 cd m^{-2}, respectively. Table S5 (ESI†) summarizes the EL characteristics of the selected PO-01-based devices reported in the literature. It is worth noting that device **BY4** with the **MS-OC**/CN-T2T mixed host exhibited a high maximum luminance, one of the highest values reported in the literature for PO-01-based devices.[34–37] On the other hand, in contrast to device **BY1**, which exhibited a high turn-on voltage of 2.9 V (defined at the luminance of 1 cd m^{-2}), devices **BY2**, **BY3**, and **BY4** exhibited extremely low turn-on voltages of approximately 2.0–2.1 V. On comparing device **BY4** with the previously reported PO-01-based devices (Table S5, ESI†) in terms of the device performance and luminance, the **MS-OC**/CN-T2T mixed host presented an outstanding balance in terms of the carrier mobility, yielding excellent performance, with high power efficiency, high maximum luminance, and low V_{on}.

Fig. 8(c) and (d) show the EQEs, luminance efficiency, and power efficiency curves, respectively, against luminance, for the **BY** series devices. The peak efficiencies for devices **BY1**, **BY2**, **BY3**, and **BY4** were respectively 15.1% (43.5 cd A^{-1} and 46.7 lm W^{-1}), 26.0% (77.2 cd A^{-1} and 109.0 lm W^{-1}), 23.6% (68.4 cd A^{-1} and 92.8 lm W^{-1}), and 27.1% (80.0 cd A^{-1} and 113.0 lm W^{-1}). Given the PLQY of the blended films mentioned above, devices **BY2**, **BY3**, and **BY4** demonstrated that carrier balance can be approximately achieved in these mixed EML structures. Notably, satisfactory efficiency together with ultra-high luminance values could be harvested in the PO-01-based device BY4 *via* a co-host of **MS-OC** and CN-T2T (**MS-OC** : CN-T2T = 1 : 1); this was attributed to the combined effect of the specific molecular and device architecture designs. Furthermore, these results indicated that the mixture of **MS-OC** and CN-T2T was even and sustained both compounds' inherent carrier transport abilities. In addition, devices **BY1**, **BY2**, **BY3**, and **BY4** exhibited efficiency drops of 26.5, 0, 0.5, and 0%, respectively, from the peak efficiency to those recorded at a practical luminance of 100 cd m^{-2}. The lower efficiency roll-off of devices **BY2–BY4** suggested mitigating TTA and stable carrier balance in the EML, mainly attributed to the mixed host enlarging the exciton formation zone.[38]

As for the **B** series device with red-emitting Ir(piq)$_2$acac, device **BR4**, which also used **MS-OC** to blend with CN-T2T for the EML, demonstrated the highest performance, as shown in Fig. S11 (ESI†). Akin to the **BY** series device, the efficiencies of the tested red-emitting devices were relative to the host materials; the lowest one was for the **MS-CN**-based device, whereas the efficiencies of devices **BR2–BR4** gradually increased. The pure

red-emitting device **BR4** exhibited a high maximum luminance of 18719 cd m^{-2} at 10.4 V and a low turn-on voltage of 2.2 V. The peak efficiency of device **BR4** reached 20.1% (12.0 cd A^{-1} and 16.6 lm W^{-1}), while a slightly lower efficiency of 18.9% (11.3 cd A^{-1} and 12.7 lm W^{-1}) was recorded at a practical luminance of 100 cd m^{-2}. However, we only investigated **MS-CN** and **MS-OC** as host materials in the green-emitting **B** series device because their triplet energy bandgaps exceeded that of Ir(ppy)$_3$. The corresponding EL characteristics of the **BG** series devices are shown in Fig. S12 (ESI†). As indicated, the green-emitting devices **BG1** and **BG4** offered very different performances, and their respective peak efficiencies reached 4.2% (12.6 cd A^{-1} and 11.3 lm W^{-1}) and 22.3% (78.2 cd A^{-1} and 111.1 lm W^{-1}). Again, **BG4** demonstrated the best performance among the tested devices, indicating that mixing **MS-OC** with CN-T2T as the host enables devices with various emitters to achieve significant carrier balance.

Regarding the performance of all the **B** series devices with mixed EMLs, most of the tested **MS-OC**-based devices with different emitters demonstrated the best performances, including high efficiency, high luminance value, low turn-on voltage, as well as mitigated efficiency roll-off. Only a few **MS-PC**-based devices exhibited the highest efficiency and luminance. A similar trend was observed for the **AR**, **AY**, **AG**, **CR**, **CY**, and **CG** series. From the molecular design and the single crystal data, the *para*-oriented **MS-PC** stacking is a phenanthrenone–phenanthrenone configuration at a distance of 4.606 Å through intermolecular π–π interactions. Additionally, the *ortho*-oriented **MS-OC** stacking is a fluorene-to-fluorene configuration with a spacing of 3.202 Å, which not only leads to the densest stacking but also demonstrates its high potential as a host material for OLED applications among four-targeted **MSs**.[24] These results demonstrate that the spiro[fluorene-9,9′-phenanthren-10′-one] core decorated with the 9-phenyl carbazole moiety in the *ortho*- or *para*-orientation could be considered an appropriate design.[39] Furthermore, this phenomenon illustrates that mixing EMLs with different synthesized compounds helps to regulate the carrier balance and increase luminance.

3. Conclusions

We have demonstrated four **MSs** based on the spiro[fluorene-9,9′-phenanthrene-10′-one] moiety as host materials, that is, **MS-CN**, **MS-TPA**, **MS-PC**, and **MS-OC**. The **MSs** have a wide energy gap, suitable energy levels and good energy level matching with Ir(ppy)$_3$, PO-01, and Ir(piq)$_2$acac emitters. Three device architectures were considered. **MS-OC** showed good performance in the device **A** series with a single EML and single host; in particular, the yellow emitter of PO-01 can be obtained with an EQE of 22.5% (67.1 cd A^{-1} and 81.1 lm W^{-1}). Device **B** series was fabricated with a co-host with the following generalized architecture: ITO (90 nm)/TAPC (30 nm)/TCTA (10 nm)/host : CN-T2T (1 : 1) doped with an emitter (25 nm)/CN-T2T (50 nm)/LiF (1.5 nm)/Al (150 nm). **MS-OC** exhibited good dense packing at the molecular level, which enhanced its charge

This journal is © The Royal Society of Chemistry 2023

J. Mater. Chem. C, 2023, **11**, 3101–3111 | **3109**

transport; consequently, it was used as a host material in the **A–C** series devices, which were superior to other **MS** series devices. In particular, **MS-OC** and CN-T2T as co-hosts for the yellow emitter PO-01 in device **BY** (*i.e.*, BY4) demonstrated the best performance with a luminance efficiency of 80.0 cd A^{-1}, power efficiency of 113.0 lm W^{-1}, and a low turn-on voltage of 2.1 V. Notably, device BY4 achieved a high maximum luminance of 142464 cd m^{-2} and an EQE of 27.1%, among the highest values reported in the literature for PO-01-based devices. These results suggest that this series of bipolar molecules are promising multifunctional materials for OLED applications.

4. Experimental section

All detailed synthesis experiment processes, OLED device fabrication, and characterizations can be found in the ESI.†

Conflicts of interest

There are no conflicts of interest to declare.

Acknowledgements

References

1 C. W. Tang and S. A. VanSlyke, *Appl. Phys. Lett.*, 1987, **51**, 913–915.

2 M. A. Baldo, S. Lamansky, P. E. Burrows, M. E. Thompson and S. R. Forrest, *Appl. Phys. Lett.*, 1999, **75**, 4–6.

3 M. Hack, M. S. Weaver and J. J. Brown, *SID Symp. Dig. Tech. Pap.*, 2017, **48**, 187–190.

4 M. A. Baldo, D. F. O'Brien, Y. You, A. Shoustikov, S. Sibley, M. E. Thompson and S. R. Forrest, *Nature*, 1998, **395**, 151–154.

5 J. Lee, J.-I. Lee, J. Y. Lee and H. Y. Chu, *Appl. Phys. Lett.*, 2009, **94**, 193305.

6 C.-H. Chang, C.-L. Ho, Y.-S. Chang, I. C. Lien, C.-H. Lin, Y.-W. Yang, J.-L. Liao and Y. Chi, *J. Mater. Chem. C*, 2013, **1**, 2639–2647.

7 Y. Seino, H. Sasabe, Y.-J. Pu and J. Kido, *Adv. Mater.*, 2014, **26**, 1612–1616.

8 C. Han, L. Zhu, J. Li, F. Zhao, Z. Zhang, H. Xu, Z. Deng, D. Ma and P. Yan, *Adv. Mater.*, 2014, **26**, 7070–7077.

9 M. Hu, Q. Xu, Y. Jiang, H. Mu, L. Gao, P. Hu, J. Huang and J. Su, *Dyes Pigm.*, 2018, **150**, 185–192.

10 H. J. Park, E. A. Chae, H. W. Seo, J.-H. Jang, W. J. Chung, J. Y. Lee, D.-H. Hwang and U. C. Yoon, *J. Mater. Chem. C*, 2020, **8**, 13843–13851.

11 C. Murawski, K. Leo and M. C. Gather, *Adv. Mater.*, 2013, **25**, 6801–6827.

12 S. Xia, R. C. Kwong, V. Adamovich, M. S. Weaver and J. J. Brown, 2007 IEEE International Reliability Physics Symposium Proceedings. 45th Annual, 2007, pp. 253–257.

13 F. So and D. Kondakov, *Adv. Mater.*, 2010, **22**, 3762–3777.

14 Y. Tao, C. Yang and J. Qin, *Chem. Soc. Rev.*, 2011, **40**, 2943–2970.

15 A. Chaskar, H.-F. Chen and K.-T. Wong, *Adv. Mater.*, 2011, **23**, 3876–3895.

16 T. Zhu and T. Van Voorhis, *J. Phys. Chem. C*, 2019, **123**, 10311–10318.

17 T. Ito, H. Sasabe, Y. Nagai, Y. Watanabe, N. Onuma and J. Kido, *Chem. – Eur. J.*, 2019, **25**, 7308–7314.

18 M.-H. Tsai, Y.-H. Hong, C.-H. Chang, H.-C. Su, C.-C. Wu, A. Matoliukstyte, J. Simokaitiene, S. Grigalevicius, J. V. Grazulevicius and C.-P. Hsu, *Adv. Mater.*, 2007, **19**, 862–866.

19 J. Jayakumar, W.-L. Wu, C.-L. Chang, T.-Y. Han, L.-Y. Ting, C.-M. Yeh, H.-W. Hung and H.-H. Chou, *Org. Electron.*, 2021, **88**, 106013.

20 Y. Zheng, A. S. Batsanov, V. Jankus, F. B. Dias, M. R. Bryce and A. P. Monkman, *J. Org. Chem.*, 2011, **76**, 8300–8310.

21 Z. Li, Z. Cheng, J. Lin, N. Xie, C. Li, G. Yang and Y. Wang, *J. Mater. Chem. C*, 2019, 7, 13486–13492.

22 N. H. Cho, J. Y. Lee, O. Y. Kim and S.-H. Hwang, *New J. Chem.*, 2020, **44**, 3868–3873.

23 Y. C. Chen, S. K. Huang, S. S. Li, Y. Y. Tsai, C. P. Chen, C. W. Chen and Y. J. Chang, *ChemSusChem*, 2018, **11**, 3225–3233.

24 Y.-M. Chang, C.-W. Li, Y.-L. Lu, M.-S. Wu, H. Li, Y.-S. Lin, C.-W. Lu, C.-P. Chen and Y. J. Chang, *ACS Appl. Mater. Interfaces*, 2021, **13**, 6450–6460.

25 W.-Y. Hung, P.-Y. Chiang, S.-W. Lin, W.-C. Tang, Y.-T. Chen, S.-H. Liu, P.-T. Chou, Y.-T. Hung and K.-T. Wong, *ACS Appl. Mater. Interfaces*, 2016, **8**, 4811–4818.

26 D. Luo, C.-W. Liao, C.-H. Chang, C.-C. Tsai, C.-W. Lu, T. C. Chuang and H.-H. Chang, *J. Phys. Chem. C*, 2020, **124**, 10175–10184.

27 Y.-T. Hung, D. Luo, L.-M. Chen, D.-C. Huang, J.-Z. Wu, Y.-S. Chen, C.-H. Chang and K.-T. Wong, *J. Mater. Chem. C*, 2022, **10**, 4748–4756.

28 C. Adachi, R. C. Kwong, P. Djurovich, V. Adamovich, M. A. Baldo, M. E. Thompson and S. R. Forrest, *Appl. Phys. Lett.*, 2001, **79**, 2082–2084.

29 H.-L. Huang, K.-H. Shen, M.-C. Jhu, M.-R. Tseng and J.-M. Liu, *Mater. Res. Soc. Symp. Proc.*, 2020, **846**, 95.

30 W.-L. Chen, S.-Y. Chen, D.-C. Huang, D. Luo, H.-W. Chen, C.-Y. Wang and C.-H. Chang, *Materials*, 2021, **14**, 5723.

31 R.-H. Yi, Y.-C. Lei, Y.-H. Tseng, Y.-F. Lin, Y.-C. Cheng, Y.-C. Fang, C.-Y. Ho, W.-W. Tsai, C.-H. Chang and C.-W. Lu, *Chem. – Eur. J.*, 2022, **28**, e202102966.

32 C.-W. Lu, C.-C. Tsai, Y.-S. Huang, H.-Y. Chih, W.-C. Li, T.-Y. Chiu and C.-H. Chang, *Dyes Pigm.*, 2019, **163**, 145–152.

33 B. Patil, J. Lade, S.-S. Chiou, Y.-C. Cheng, Y.-F. Lin, Y. Jadhav, P. Chetti, C.-H. Chang and A. Chaskar, *Org. Electron.*, 2021, **92**, 106090.

3110 | *J. Mater. Chem. C*, 2023, **11**, 3101–3111

This journal is © The Royal Society of Chemistry 2023

34 M. Kim and J. Y. Lee, *Synth. Met.*, 2015, **199**, 105–109.

35 K. Gao, K. Liu, X.-L. Li, X. Cai, D. Chen, Z. Xu, Z. He, B. Li, Z. Qiao, D. Chen, Y. Cao and S.-J. Su, *J. Mater. Chem. C*, 2017, **5**, 10406–10416.

36 C. Cao, W.-C. Chen, J.-X. Chen, L. Yang, X.-Z. Wang, H. Yang, B. Huang, Z.-L. Zhu, Q.-X. Tong and C.-S. Lee, *ACS Appl. Mater. Interfaces*, 2019, **11**, 11691–11698.

37 B. Sun, K.-N. Tong, X. Chen, J.-L. He, H. Liu, M.-K. Fung and J. Fan, *J. Mater. Chem. C*, 2021, **9**, 7706–7712.

38 Y. Chen, J. Chen, Y. Zhao and D. Ma, *Appl. Phys. Lett.*, 2012, **100**, 213301.

39 R.-H. Yi, C.-M. Shao, C.-H. Lin, Y.-C. Fang, H.-L. Shen, C.-W. Lu, K.-Y. Wang, C.-H. Chang, L.-Y. Chen and Y.-H. Chang, *J. Phys. Chem. C*, 2020, **124**, 20410–20423.